Structural and magnetic ordering in $La_{0.5}Ca_{0.5-x}Ba_xMnO_3$ $(0 < x \leq 0.5)$ manganite

Structural and magnetic ordering in La$_{0.5}$Ca$_{0.5-x}$Ba$_x$MnO$_3$ (0 < x ≤ 0.5) manganite

Indu Dhiman[1], **A Das**[1] **and A K Nigam**[2]

[1] Solid State Physics Division, Bhabha Atomic Research Centre, Mumbai 400085, India
[2] Tata Institute of Fundamental Research, Colaba, Mumbai 400005, India

E-mail: adas@barc.gov.in

Abstract

We report a structural, magnetic and transport study in La$_{0.5}$Ca$_{0.5-x}$Ba$_x$MnO$_3$ (0 < x ≤ 0.5) using neutron diffraction, magnetization and resistivity measurements. The samples crystallize in an orthorhombic structure with *Pnma* space group and no structural transition is observed with Ba doping. Substituting Ca with Ba leads to an increase in average A-site ionic radii, $\langle r_A \rangle$ and cation size disorder (σ^2). Consequently, the nature of magnetic ordering undergoes changes as a function of x. At low temperature for $x \leqslant 0.1$, the CE-type antiferromagnetic spin structure is stabilized, similar to the parent compound. At $x = 0.15$, the magnetic phase is a mixture of CE-type and A-type spin structure. For $x \geqslant 0.2$, the ferromagnetic phase is stabilized. The signature of orbital ordering in addition to spin and charge ordering is observed in all samples with $x \leqslant 0.15$. T_C, T_{CO} and T_N remain nearly constant for $x \leqslant 0.2$. The transport studies reveal that for samples $x \leqslant 0.2$, adiabatic hopping of small polarons governs the transport behaviour above T_{CO} ($\sim$160 K). A parallel combination of small polaron hopping and variable range hopping mechanisms is found to describe resistivity data below T_{CO}. At $x = 0.2$, an insulator to metal transition is observed as temperature is lowered, and at $x = 0.5$ the sample becomes metallic below 280 K. In the metallic regime, resistivity data follows the Bloch–Grüneisen model together with contributions from high frequency optical phonons and magnetic scattering. The experimentally established phase diagram from the present study is compared with theoretical studies in the intermediate electron–phonon interaction regime.

1. Introduction

The doped manganites RE$_{1-x}$A$_x$MnO$_3$ (RE = trivalent rare earth, A = divalent alkaline earth ion Ca, Sr and Ba) have been widely studied as a result of interesting transport and magnetic properties displayed by these compounds. Upon substitution of a divalent alkaline earth ion for a trivalent rare earth ion on the A site, a certain percentage of Mn^{3+} is replaced by Mn^{4+}. Thus, the substitution provides free carriers for conduction. Depending upon doping and A-site ionic radii, these compounds exhibit various magnetic ground states such as ferromagnetic metallic, antiferromagnetic insulating, charge ordering, orbital ordering and colossal magnetoresistance (CMR) as a function of temperature [1]. The system La$_{1-x}$Ca$_x$MnO$_3$ exhibits a complex phase diagram as a function of doping and temperature [2]. At a composition

$x = 0.5$, which is our interest here, there is a coexistence of many ordered phases such as charge, orbital and spin ordering as a function of temperature [3]. This system undergoes successive ferromagnetic metallic transitions below $T_C \sim$ 230 K and CE-type antiferromagnetic insulating transitions below $T_N \sim$ 170 K. It has been observed that, if charge ordering is accompanied with antiferromagnetic transition, the spin structure is of CE-type.

In half-doped manganites, as a consequence of the 1:1 ordering of Mn^{3+}/Mn^{4+}, the charge ordering is most stable for a doping level at $x = 0.5$. The charge ordering behaviour and the consequent magnetic structure may be influenced by magnetic field, or external or internal pressure by substituting at the RE or transition metal site. In particular, substituting at the A site is found to modify the magnetic properties considerably. The resulting difference in ionic radii

between the RE^{3+} and A^{2+} leads to a disorder effect which is given by an expression, $\sigma^2 = \sum x_i r_i^2 - \langle r_A \rangle^2$, where x_i denotes the fractional occupancy of the A-site ion and r_i is the corresponding ionic radius and $\langle r_A \rangle$ is the average A-site ionic radius [4]. In general, the influence of $\langle r_A \rangle$ on the magnetic properties depends upon the $\langle r_A \rangle$ regime under consideration. The changes in magnetic properties as a result of change in $\langle r_A \rangle$ are attributed to either change in one-electron bandwidth W or disorder (σ^2). On the basis of variation in W these compounds may be classified into three different regimes: (1) low $\langle r_A \rangle$ ($\langle r_A \rangle$ < 1.18 Å), (2) intermediate $\langle r_A \rangle$ (1.18 Å < $\langle r_A \rangle$ < 1.252 Å) and (3) high $\langle r_A \rangle$ ($\langle r_A \rangle$ > 1.252 Å) [5]. In the low $\langle r_A \rangle$ regime, the charge ordered state is highly stable and no ferromagnetism is observed. The systems $RE_{0.5}Ca_{0.5}MnO_3$ with RE = Nd, Pr, Sm are in the low $\langle r_A \rangle$ regime. In the intermediate regime, competing ferromagnetic and antiferromagnetic phases are observed with charge and orbital ordering. The compounds $La_{0.5}Ca_{0.5}MnO_3$, $Nd_{0.5}Sr_{0.5}MnO_3$ and $Pr_{0.5}Sr_{0.5}MnO_3$ belong to this regime. The high $\langle r_A \rangle$ regime has compounds which are ferromagnetic metallic down to the lowest temperature such as the $La_{0.5}Sr_{0.5}MnO_3$ and $La_{0.5}Ba_{0.5}MnO_3$ systems. This indicates that a variety of magnetic structures are observed in half-doped compounds as a result of variation in $\langle r_A \rangle$. However, the role of disorder in influencing the magnetic structure in half-doped manganites with coexisting ferromagnetic and antiferromagnetic phases as found in compounds in the intermediate $\langle r_A \rangle$ regime have not been as extensively studied as compared to the studies in the ferromagnetic systems [4, 6–12].

In the present paper, we study the effect of substituting Ca with Ba in $La_{0.5}Ca_{0.5}MnO_3$. The substitution results in an increase in $\langle r_A \rangle$ and σ^2 due to the higher ionic radius of 1.47 Å for Ba as compared to the Ca ion of 1.18 Å [13]. Previously, we have reported a similar effect of varying $\langle r_A \rangle$ and effectively increasing disorder on the system $La_{0.5}Ca_{0.5-x}Sr_xMnO_3$ [14]. We observed that increasing $\langle r_A \rangle$ leads to destabilization of CE-type antiferromagnetic, charge ordered and orbitally ordered states. The CE type of antiferromagnetic ordering is followed by an A-type charge disordered but orbitally ordered phase, before the ferromagnetic metallic state is stabilized with further increase in $\langle r_A \rangle$. However, the disorder was not as high as in the present $La_{0.5}Ca_{0.5-x}Ba_xMnO_3$ series. In this series of compounds, the variation of disorder from 3.24×10^{-4} for $x = 0$ to 1.62×10^{-2} for $x = 0.5$ is significantly higher than other series of compounds reported previously [15–22].

Previously reported magnetic and transport studies on $La_{0.5}Ca_{0.5-x}Ba_xMnO_3$ compounds have shown that Ba substitution leads to stabilization of an antiferromagnetic insulating state [23]. This behaviour is attributed to the cation size disorder σ^2. This is contrary to the expected behaviour, wherein the increase of $\langle r_A \rangle$ leads to a ferromagnetic metallic state. These observations are not in agreement with the study of Yuan *et al* [24]. They report that, for $x \geqslant 0.14$, the system displays a metal to insulator transition. The metal to insulator transition temperature increases with doping. Similarly, Mallik *et al* report an increase in metal–insulator transition temperature with increase in x. However,

magnetic susceptibility studies show non-monotonic variation of T_C as a function of increasing Ba concentration, and is attributed to disorder [25]. These studies suggest that current understanding of the effect of large disorder on magnetic structure, in particular in intermediate bandwidth compounds, is inconclusive.

The phase separation behaviour observed in these compounds has also attracted great theoretical interest [26]. Theoretically, the appearance of a charge ordered CE-type antiferromagnetic ground state in half-doped manganites with smaller $\langle r_A \rangle$ could not be reproduced by a simple double exchange model. The introduction of electron–phonon coupling terms due to cooperative or non-cooperative Jahn–Teller phonons was found to be necessary for the construction of the phase diagram of half-doped manganites with CO–OO–CE-type AFM states [27, 28]. The effect of variation of the A-site ionic radii as a result of random chemical replacement of ions such as Ca^{2+} with Ba^{2+} is identified with quenched disorder. In the presence of quenched disorder the hopping of e_g electrons and the exchange J_{AF} between t_{2g} spins is affected due to buckling of Mn–O–Mn bonds. Taking into account the fluctuations of hopping and exchange couplings, Monte Carlo studies in these compounds reveal the coexistence of giant clusters of ferromagnetic and antiferromagnetic phases [29]. Variation of disorder can lead to preferential stabilization of one phase as compared to the other. In a similar study, which included the electron–phonon coupling (λ), CE-type and A-type antiferromagnetic and ferromagnetic phases were realized as a function of λ and J_{AF} [30]. We find substituting Ba for Ca in these half-doped compounds is similar to variation of J_{AF} for a given λ. In this paper we attempt to describe the influence of quenched disorder on the resistivity, magnetization and magnetic structure of half-doped intermediate bandwidth manganites.

2. Experiment

The samples were synthesized by the conventional solid-state reaction method. The starting materials La_2O_3, MnO_2, $BaCO_3$ and $CaCO_3$ were mixed in stoichiometric ratio and held for 24 h at 1350 °C for calcination. Samples were removed and sintered at 1450 °C for 24 h with intermediate grinding. Finally, the samples were pelletized and heat treated at 1450 °C for 24 h. Initial values of cell parameters for all the samples were obtained from x-ray powder diffraction recorded on a Rigaku diffractometer, using Cu Kα radiation in the angular range, $10° \leqslant 2\theta \leqslant 70°$. For higher concentrations of Ba ($x \geqslant 0.3$), the $BaMnO_3$ impurity phase is present. This extra phase is accounted for in neutron diffraction studies. Neutron diffraction patterns were recorded on a multi-PSD-based powder diffractometer ($\lambda = 1.249$ Å) at the Dhruva reactor, Bhabha Atomic Research Centre, Mumbai at selected temperatures between 22 and 300 K in the $5° \leqslant 2\theta \leqslant 140°$ angular range. The powdered samples were packed in a cylindrical vanadium container and attached to the cold finger of a closed-cycle helium refrigerator. Rietveld refinement of the neutron diffraction patterns was carried out using the FULLPROF program [31]. The magnetization

Table 1. Structural parameters obtained from Rietveld refinement of neutron diffraction pattern at 300 K for samples $La_{0.5}Ca_{0.5-x}Ba_xMnO_3$. The atomic sites are: La/Ca/Ba 4c $(x, 1/4, z)$; Mn 4a$(0, 0, 0)$; O(1) 4c $(x, 1/4, z)$; O(2) 8d (x, y, z) in *Pnma* space group. The symbol O_1 denotes the oxygen atom along the *b* axis (apical) and O_{21} and O_{22} are the two oxygen atoms in the *ac* plane (equatorial).

Refined parameters	$x = 0.05$	$x = 0.1$	$x = 0.15$	$x = 0.2$	$x = 0.3$	$x = 0.4$	$x = 0.5$
a (Å)	5.413(2)	5.435(3)	5.436(2)	5.455(1)	5.4807(8)	5.5021(7)	5.508(1)
b (Å)	7.640(3)	7.647(2)	7.647(1)	7.702(2)	7.769(1)	7.789(1)	7.790(2)
c (Å)	5.439(2)	5.444(3)	5.463(1)	5.491(1)	5.4560(7)	5.4814(5)	5.530(1)
V (Å^3)	224.9(1)	226.2(2)	227.11(8)	230.7(1)	232.33(6)	234.90(5)	237.3(1)
La/Ca/Ba							
x	−0.001(10)	0.004(13)	−0.002(3)	−0.0003(20)	0.004(5)	−0.004(2)	0.004(3)
z	0.498(6)	0.497(3)	0.498(3)	0.494(1)	0.484(3)	0.498(3)	0.501(6)
O(1)							
x	0.51(2)	0.51(1)	0.518(4)	0.530(3)	0.509(9)	0.509(3)	0.508(4)
z	0.547(5)	0.549(3)	0.542(2)	0.547(2)	0.521(2)	0.511(3)	0.507(74)
O(2)							
x	0.255(8)	0.260(1)	0.260(4)	0.266(2)	0.258(9)	0.253(3)	0.259(2)
y	0.025(2)	0.023(2)	0.024(1)	0.021(8)	0.017(8)	0.015(8)	0.011(1)
z	0.235(6)	0.245(1)	0.251(8)	0.242(3)	0.240(3)	0.245(5)	0.246(7)
Mn–O$_1$ (Å)	1.927(4)	1.931(5)	1.927(2)	1.950(2)	1.946(1)	1.9491(7)	1.949(1)
Mn–O$_{21}$ (Å)	1.90(4)	1.95(6)	1.99(4)	1.97(1)	1.93(2)	1.94(3)	1.99(2)
Mn–O$_{22}$ (Å)	1.97(4)	1.91(7)	1.89(4)	1.91(1)	1.95(2)	1.95(3)	1.92(2)
Mn–O$_1$–Mn (deg)	165.04(15)	163.8(12)	165.43(8)	162.0(8)	172.58(5)	175.41(3)	175.58(5)
Mn–O$_2$–Mn (deg)	167.3(2)	169.0(3)	169.0(1)	168.8(6)	171.2(8)	173.0(11)	173.5(10)

measurements were carried out on a superconducting quantum interference design (SQUID) magnetometer and vibrating sample magnetometer (VSM). The zero-field (ZFC) and field-cooled (FC) measurements were performed under a magnetic field of 10 kOe. The dc resistivity measurements between 3 and 300 K were performed by a standard four-probe technique.

## 3. Results and discussion

3.1. Crystal structure and distortions

All the samples in the $La_{0.5}Ca_{0.5-x}Ba_xMnO_3$ ($0 < x \leqslant 0.5$) series are isostructural. They crystallize in orthorhombic structure with space group *Pnma*. No structural transition has been observed on lowering temperature. This is in agreement with earlier findings [3]. The structural parameters were obtained from Rietveld refinement of neutron diffraction patterns at various temperatures and the parameters obtained at 300 and 22 K are given in tables 1 and 2, respectively. The unit-cell volume increases with Ba doping from 224 Å^3 for $x = 0$ to 237 Å^3 for $x = 0.5$, due to larger ionic radii of Ba ions in comparison to Ca ions. Figure 1 displays the distortion parameter D and disorder σ^2 as a function of Ba concentration. The $\langle r_A \rangle$ increases linearly with x, while σ^2 displays a maximum at $x = 0.4$. The distortion parameter D is defined as $D = \frac{1}{3} \sum_i \frac{a_i - \langle a \rangle}{\langle a \rangle} 100$, where $a_1 = a$, $a_2 = b/\sqrt{2}$ and $a_3 = c$ are the cell parameters and $\langle a \rangle$ is the average value of the cell parameters [32]. The distortion parameter represents a combination of JT-type, shear type and tilt distortions. It is observed that, as a function of x, the distortion parameter displays a maximum at $x = 0.15$ ($\langle r_A \rangle \approx 1.24$ Å). A similar feature was also observed in Sr-doped samples [14] and in other half-doped manganites [33]. The orthorhombic *Pnma* symmetry is obtained from the undistorted cubic perovskite structure by rotations of the octahedra anti-phase about the *a*

and *c* axes and in-phase about the *b* axis. The in-phase and anti-phase rotations are denoted by Glazer with the superscripts + and −, respectively, such that the symbol associated with the *Pnma* space group is $a^-b^+a^-$ [34, 35]. Treating MnO$_6$ as a non-rigid octahedron, Kennedy *et al* [36] proposed a method to estimate in-phase and out-of-phase tilting of these octahedra, using the positional parameter of equatorial O(2) atoms. The out-of-phase tilt angles along the diad axis thus estimated show a large decrease, reducing from 8° for $x = 0.05$ to 3.5° for a $x = 0.5$ compound sample, while the in-phase tilt angle about the *b* axis does not exhibit much change (3°±1°). For $x = 0.5$, the distortion of MnO$_6$ octahedra is considerably reduced and the system tends towards a cubic structure. At 300 K, the A-site disordered compound $La_{0.5}Ba_{0.5}MnO_3$ has been previously described using cubic $Pm\bar{3}m$ space group [21]. However, in our case, we obtain the best fit with the orthorhombic structure. It is observed that for orthorhombic phase (S. G. *Pnma*), the $\chi^2 = 3.57$, whereas for cubic phase (S. G. $Pm\bar{3}m$) the $\chi^2 = 4.35$ implying that an orthorhombic structure is a better fit than the cubic structure. Similarly, fits were tried with $R\bar{3}c$ and $I4/mcm$ space groups. These too yield poor fits with several unindexed reflections. This gives an indication that, for sample $La_{0.5}Ba_{0.5}MnO_3$ (0.5), the structure is orthorhombic. However, it is observed that the intensity of the (1 1 2) (2 1 1) reflection reduces with increasing x. This is an indication that the system is evolving towards a cubic phase. Our results are in agreement with Mallik *et al* [25].

The orthorhombic cell parameters are related to those of the ideal cubic subcell as $a \approx c \approx \sqrt{2}a_0$ and $b \approx 2a_0$ ($a_0 \sim 3.8$ Å). The distortion to an orthorhombic structure will lead to such a change of cell parameters from the ideal cubic cell. There are two types of structures related to orthorhombic symmetry denoted as O′ and O orthorhombic structure. All the compounds having $x \leqslant 0.4$ crystallize with the perovskite structure at 300 K having the O′ orthorhombic ($b/\sqrt{2} <$

Table 2. Structural parameters obtained from Rietveld refinement of neutron diffraction pattern at 22 K for samples $La_{0.5}Ca_{0.5-x}Ba_xMnO_3$. The atomic sites are: La/Ca/Ba 4c (x, 1/4, z); Mn 4a (0, 0, 0); O(1) 4c (x, 1/4, z); O(2) 8d (x, y, z) in *Pnma* space group. The symbol O_1 denotes the oxygen atom along the b axis (apical) and O_{21} and O_{22} are the two oxygen atoms in the *ac* plane (equatorial).

Refined parameters	$x = 0.05$	$x = 0.1$	$x = 0.15$	$x = 0.2$	$x = 0.3$	$x = 0.4$	$x = 0.5$
a (Å)	5.426(1)	5.440(1)	5.436(2)	5.443(1)	5.4710(8)	5.4892(8)	5.499(1)
b (Å)	7.536(2)	7.536(2)	7.647(1)	7.693(2)	7.7533(9)	7.7762(9)	7.772(1)
c (Å)	5.474(1)	5.486(1)	5.463(1)	5.485(1)	5.4470(6)	5.4689(6)	5.5211(6)
V (Å^3)	223.8(1)	224.93(8)	225.87(7)	229.7(1)	231.05(5)	233.44(5)	235.97(6)
La/Ca/Ba							
x	−0.003(16)	−0.003(2)	0.0004(40)	−0.002(5)	−0.006(5)	−0.003(3)	−0.001(2)
z	0.497(3)	0.499(3)	0.495(2)	0.497(2)	0.491(2)	0.495(2)	0.499(4)
Mn							
$M_{Mn^{3+}}$ CE−type AFM (μ_B)	1.1(2)	1.8(2)	0.98(20)	—	—	—	—
$M_{Mn^{4+}}$ CE−type AFM (μ_B)	2.1(2)	2.1(2)	1.9(3)	—	—	—	—
$M_{A-type\ AFM}$ (μ_B)	—	—	1.53(5)	—	—	—	—
M_{FM} (μ_B)	—	—	—	3.67(8)	3.10(7)	3.62(6)	3.59(7)
O(1)							
x	0.497(1)	0.492(1)	0.525(4)	0.506(9)	0.500(8)	0.509(5)	0.511(3)
z	0.548(3)	0.548(2)	0.551(2)	0.535(2)	0.532(1)	0.523(2)	0.526(2)
O(2)							
x	0.254(1)	0.250(10)	0.261(3)	0.262(2)	0.258(3)	0.255(2)	0.255(3)
y	0.027(1)	0.027(1)	0.026(8)	0.025(8)	0.016(1)	0.014(6)	0.007(1)
z	0.236(3)	0.235(3)	0.241(3)	0.239(2)	0.239(2)	0.245(5)	0.249(7)
Mn–O_1 (Å)	1.903(3)	1.903(2)	1.911(2)	1.933(2)	1.947(7)	1.9487(9)	1.949(1)
Mn–O_{21} (Å)	1.89(3)	1.88(4)	1.95(2)	1.95(1)	1.92(2)	1.94(2)	1.96(3)
Mn–O_{22} (Å)	1.99(3)	2.00(4)	1.94(2)	1.94(1)	1.95(2)	1.94(2)	1.93(3)
Mn–O_1–Mn (deg)	163.9(1)	164.06(7)	161.37(9)	168.44(5)	169.52(4)	172.11(4)	170.83(4)
Mn–O_2–Mn (deg)	167.3(13)	167.6(17)	167.6(7)	167.3(5)	173.6(9)	173.1(9)	176.3(12)
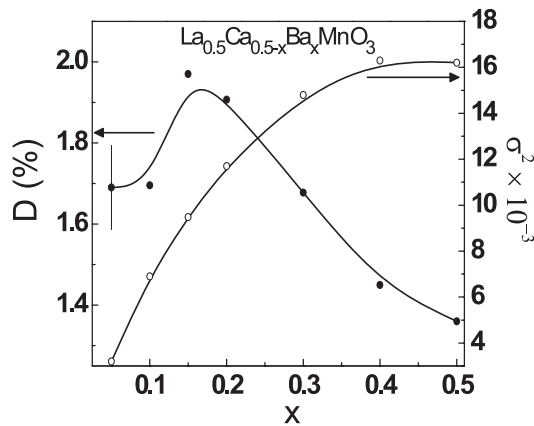
Figure 1. A plot of distortion (D) and disorder σ^2 as a function of x at 300 K for the $La_{0.5}Ca_{0.5-x}Ba_xMnO_3$ series. The error values in D (%) are estimated to be ∼6%.

$a < c$) symmetry. In this structure a cooperative Jahn–Teller distortion superimposes on the rotation of the MnO_6 octahedra. This induces an orbital ordering and distorts the MnO_6 octahedra. The O orthorhombic structure is due to cooperative buckling of the corner-shared octahedra. This structure is purely due to the rotation of octahedra [37, 38]. For composition $x = 0.5$, the cell parameter a and $b/\sqrt{2}$ are nearly equal to each other, which could indicate that the system is tending towards O orthorhombic structure.

Figures 2–4 shows the temperature dependence of (a) cell parameters (b) bond lengths (c) bond angles (d) magnetization and (e) resistivity for samples $x = 0.1$, 0.2 and 0.5,

respectively. The figures display a close coupling between the structural, magnetic and physical properties and their varied nature as a function of x. The temperature dependence of cell parameters shown in figure 2(a) is a representation of all the samples having $x \leqslant 0.15$. On lowering temperature, lattice parameters exhibit anomalous behaviour for samples between $0.05 \leqslant x \leqslant 0.15$, as observed for parent and various other charge ordered systems, exhibiting orbital ordering [35]. The (2 0 2) and (0 4 0) reflections in the neutron diffraction pattern for samples $x = 0.1$ and 0.15 were merged at 300 K. This reflection exhibits a splitting (figure 6) and the temperature below which this splitting is observed coincides with the charge ordering temperature in this case. The lattice parameter b shrinks drastically, while the a and c parameters expand. This behaviour is observed normally in systems exhibiting CE-type antiferromagnetic ordering and is associated with orbital ordering of the $d_{z^2}^2$ orbital in the a–c plane [3]. At $x = 0.15$, the nature of orbital ordering is similar to samples having $x \leqslant 0.10$, though this sample is a mixture of CE-and A-type antiferromagnetic spin structure as discussed later. For samples having $x \geqslant 0.2$, the cell parameters do not show any anomalous behaviour, giving indirect evidence for the absence of orbital ordering.

From the estimated bond lengths and bond angles we calculate the one-electron bandwidth W of e_g electrons using the formula, $W \alpha \frac{\cos \frac{1}{2}(\pi - \langle \theta \rangle)}{d^{3.5}}$. where $\langle \theta \rangle$ is the average Mn–O–Mn bond angle and d is the average Mn–O bond length [39]. The bandwidth W remains nearly constant within error bars. The bandwidth variation therefore does not explain the onset of long range ferromagnetic ordering and metallic behaviour with progressive substitution of Ba in these compounds. Similar
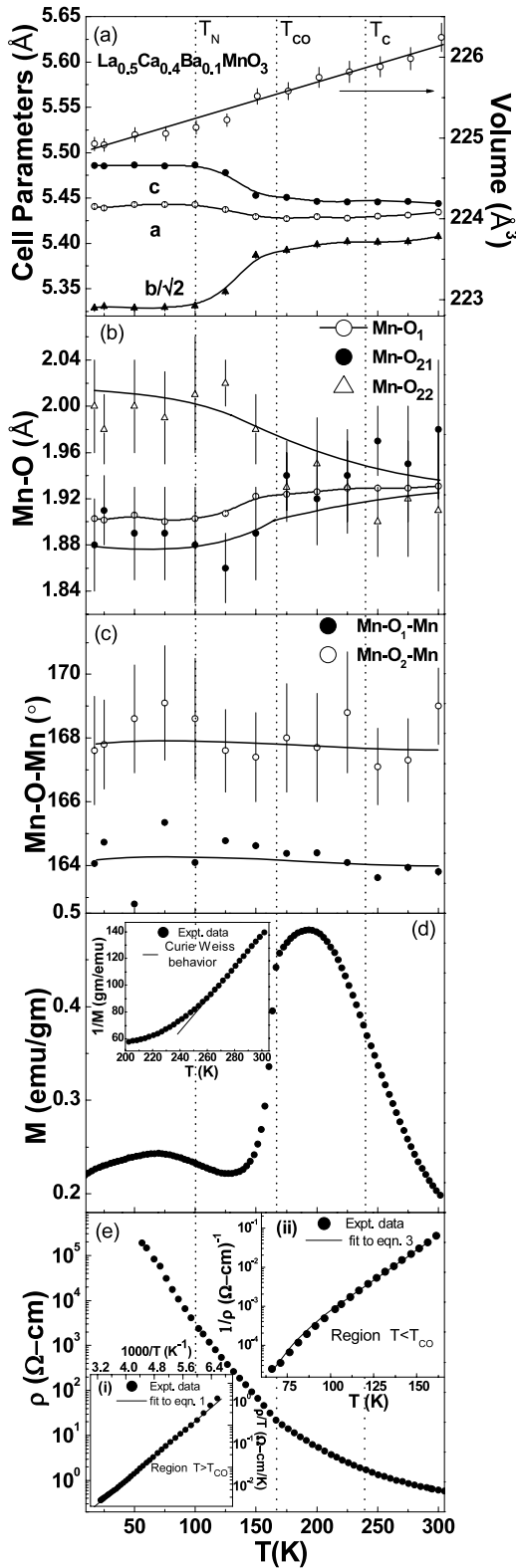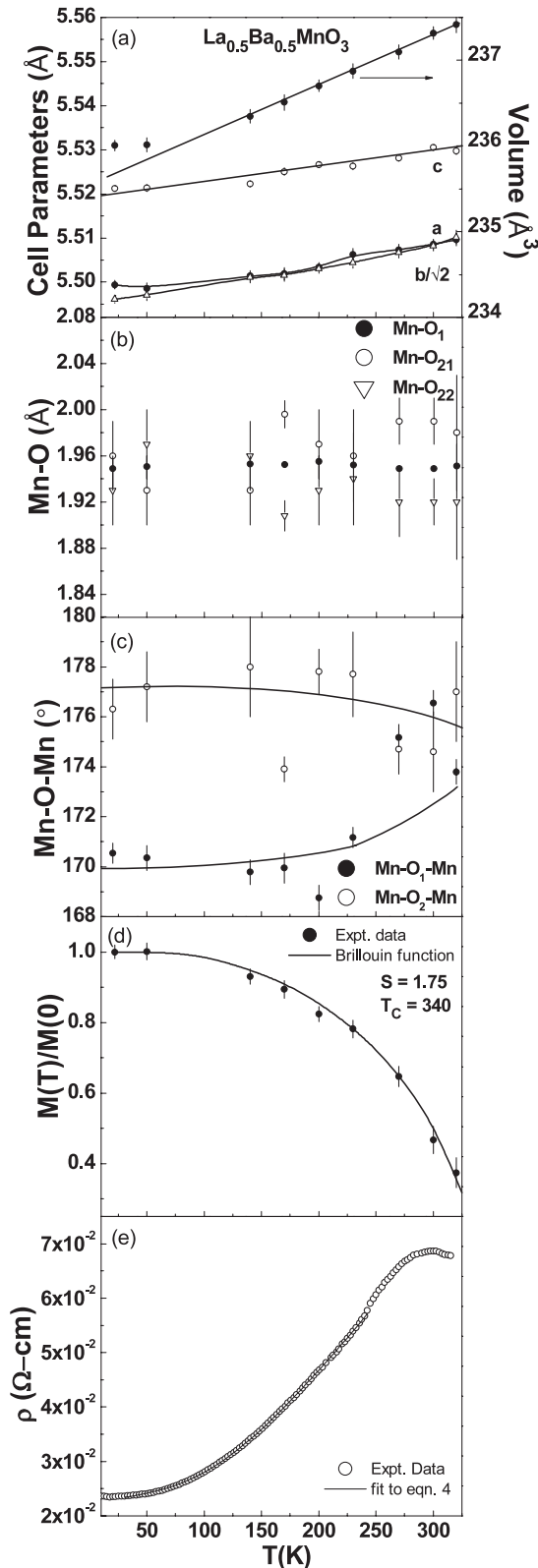
Figure 2. (a) Temperature dependence of lattice parameters and the unit-cell volume for the La$_{0.5}$Ca$_{0.4}$Ba$_{0.1}$MnO$_3$ ($x = 0.1$) sample. (b) Bond lengths as a function of temperature are shown. (c) Bond angles as a function of temperature. The continuous lines are a guide for the eyes. (d) Variation of magnetization with temperature and the inset shows the inverse of magnetization with temperature; the continuous line is a linear fit to the Curie–Weiss equation. (e) Temperature dependence of resistivity. Inset (i) shows a fit to the resistivity data to equation (1) above T_{CO} and inset (ii) shows a fit to equation (3) below T_{CO}.
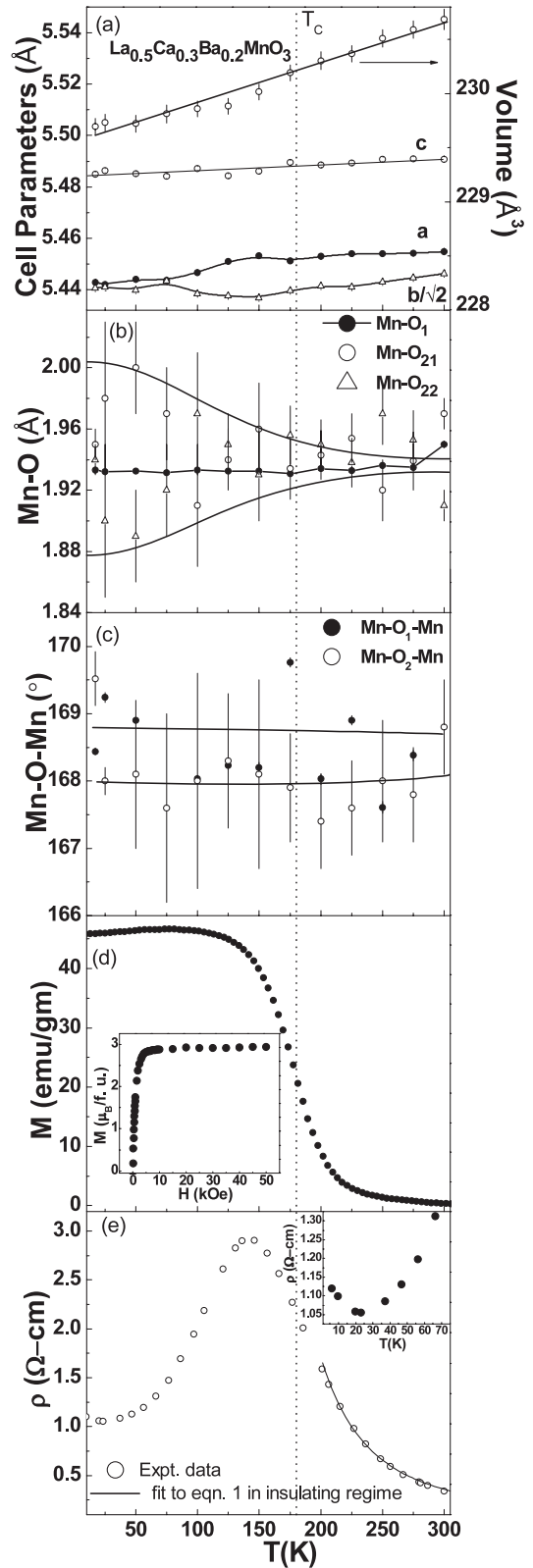
Figure 3. (a) Temperature dependence of lattice parameters and the unit-cell volume for the La$_{0.5}$Ca$_{0.3}$Ba$_{0.2}$MnO$_3$ ($x = 0.2$) sample. (b) Bond lengths as a function of temperature are shown. (c) Bond angles as a function of temperature. The continuous lines are a guide for the eyes. (d) Variation of magnetization with temperature and the inset shows the variation of magnetization (M) with field (H) at 5 K. (e) Temperature dependence of resistivity. The inset shows low temperature resistivity minimum observed. The continuous line is fitted to the resistivity data.

Figure 4. (a) Temperature dependence of lattice parameters and the unit-cell volume for the La$_{0.5}$Ba$_{0.5}$MnO$_3$ ($x = 0.5$) sample. (b) Bond lengths as a function of temperature are shown. (c) Bond angles as a function of temperature. The continuous lines are a guide for the eyes. (d) The variation of ferromagnetic moment with temperature as obtained from Rietveld analysis of neutron diffraction patterns at various temperatures. The continuous line displays a Brillouin function fit. (e) Temperature dependence of resistivity is shown. The continuous line shows a fit to equation (4).

observations where the electronic bandwidth W has little role in the varied magnetic properties, has been reported earlier [40].

The evolution of Mn–O bond distances as a function of temperature for samples $x = 0.1$, 0.2 and 0.5 is shown in figures 2(b), 3(b) and 4(b), respectively. For samples having $x \leqslant 0.2$, the difference between the three Mn–O bond lengths increases with reducing temperature. This indicates an increase in JT distortions on lowering of temperature. For the $x = 0.2$ sample, the temperature dependence of Mn–O bond lengths is similar to that of samples having $x < 0.2$, despite the ferromagnetic nature of the sample. For samples having $x \geqslant 0.3$, the Mn–O bond lengths are very close to each other down to 22 K. Figure 4(b) shows evolution of bond length with temperature for the compound $x = 0.5$. The Mn–O bond lengths remain nearly constant with temperature, indicating the suppression of JT distortion in the ferromagnetic state. The temperature dependence of bond angles for samples $x = 0.1$, 0.2 and 0.5 is shown in figures 2(c), 3(c) and 4(c), respectively. The Mn–O–Mn bond angles remain nearly constant with temperature for all the samples.

On lowering temperature below T_{CO}, a structural transition has been reported for the $x = 0$ compound [3]. The model for charge ordered phase was proposed by Goodenough [41]. This model assumes that localized Mn^{3+} and Mn^{4+} states order in alternate planes. The $Pnma$ superstructure contains only one symmetry-equivalent Mn site and so does not describe long range CO. Lowering of symmetry to $P2_1/m$ space group is used to accommodate the ordering of Mn^{3+} and Mn^{4+} ions on two inequivalent sites instead of a single site available in the space group $Pnma$. However, lowering of space group to $P2_1/m$ necessarily requires inclusion of 31 positional parameters as against 7 positional parameters in the case of $Pnma$. In this case the refinement becomes unstable and the obtained parameters are less reliable in the absence of good quality synchrotron data. Such a conclusion in the case of $x = 0$ has been arrived at from analysis of synchrotron data, though the neutron data in the charge ordered state was still described in the $Pnma$ space group. We have followed a similar procedure of analysing low temperature neutron data in the $Pnma$ space group, though a lower symmetry structure would have been more appropriate in charge ordered systems. Our analysis yields an averaged structure and consequently the obtained Mn–O bond lengths and Mn–O–Mn angles give the averaged values for two Mn sites.
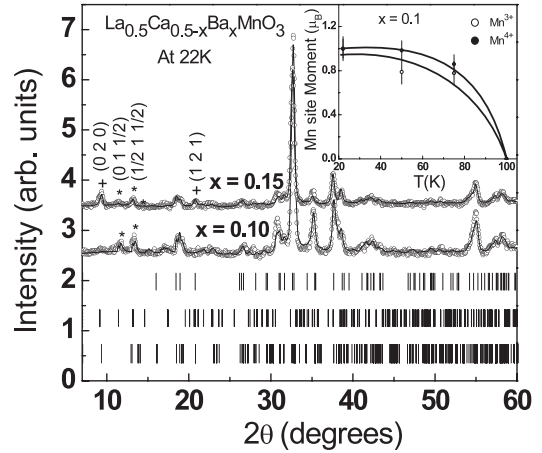
3.2. Magnetization and transport properties

Magnetization as a function of temperature for compound $x = 0.1$ is shown in figure 2(d). For all samples having $x \leqslant 0.15$, magnetization displays a similar temperature dependence, as for the $x = 0.1$ compound. Magnetization was measured as a function of temperature in the zero-field-cooled (ZFC) condition. The variation in magnetization with temperature for samples $0.05 \leqslant x \leqslant 0.15$ is similar to that observed in the case of $x = 0$ [42]. An increase in magnetization is observed as temperature is lowered below 300 K, attributable to the onset of ferromagnetic ordering. The maximum in magnetization at
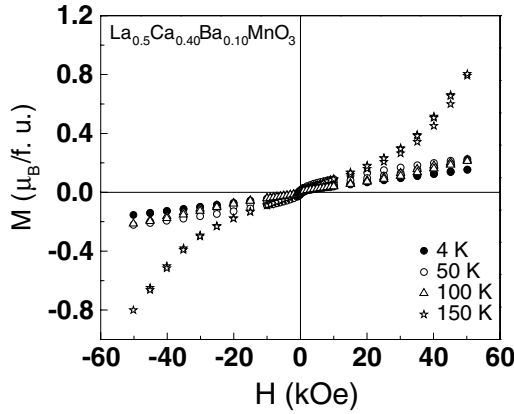
Figure 5. Variation of magnetization (M) with field (H) for sample La$_{0.5}$Ca$_{0.4}$Ba$_{0.1}$MnO$_3$ ($x = 0.10$) at 4, 50, 100 and 150 K.

Figure 6. Neutron diffraction pattern recorded on sample La$_{0.5}$Ca$_{0.5-x}$Ba$_x$MnO$_3$ ($x = 0.1$ and 0.15) at 22 K. Continuous lines through the data points are the fitted lines to the chemical and magnetic structure described in the text. The symbol ($*$) indicates the CE-type antiferromagnetic reflection and ($+$) indicates reflection corresponding to the A-type AFM reflections. The tick marks in the first, second and third rows correspond to positions of Bragg reflections in nuclear, CE-type AFM and A-type AFM phases, respectively. The inset shows the variation of antiferromagnetic site moment of Mn^{3+} and Mn^{4+} ions with temperature for sample $x = 0.1$. The continuous lines are a guide for the eyes.

about 175 K is indicative of ferromagnetism in these samples. On lowering temperature further, another weak maximum in magnetization is observed at $\sim$75 K. From neutron diffraction data described later, we identify this weak maximum at $\sim$75 K with the transition to an antiferromagnetic state in this compound. In the range $T < T_N$ coexistence of ferromagnetic nanoclusters and charge ordered antiferromagnetic phases is evident from a narrow hysteresis loop observed in $M(H)$ behaviour shown in figure 5. The magnetization values are far below the expected value of the magnetic moment of the Mn^{3+} and Mn^{4+} mixture. On increasing the temperature close to T_C the high field magnetization increases. Such an increase in moment values with increasing temperature is in agreement with the $M(T)$ observed in these samples and indicate growth of ferromagnetic clusters. Similar behaviour has been observed previously in Sr-doped samples [14]. Coexistence of ferromagnetic and antiferromagnetic clusters have been reported in the parent compound [43]. The ferromagnetic transition temperatures T_C, for all the samples were obtained from the minimum in the dM/dT versus T plot. The T_C ($\sim$235 K) remains nearly constant for composition $0 \leqslant x \leqslant 0.15$. At $x = 0.2$, the antiferromagnetic nature is totally suppressed and the sample exhibits ferromagnetic behaviour on lowering temperature, as shown in figure 3(d). For $x = 0.2$, T_C reduces to $\sim$180 K, which is in agreement with our neutron diffraction study. The signature of typical ferromagnetic behaviour is evident from $M(H)$ curves of samples $x \geqslant 0.2$. $M(H)$ shows a sharp rise in M at low field and saturates thereafter, as shown in the inset of figure 3(d). The saturation value of magnetization is close to the expected value of 3.5 μ_B/f.u. In previously reported magnetization studies on the similar series, the ferromagnetic transition temperature for sample $x = 0.1$ is $\sim$120 K, which is not in agreement with the present study [25]. However, for the sample with $x = 0.2$ it is in relatively good agreement with the value of $T_C \sim 200$ K, reported by Mallik *et al* [25]. We have fitted the magnetization data in the temperature range 250 K $< T <$ 300 K to a Curie–Weiss law. The inset of figure 2(d) shows the inverse of magnetization as a function of temperature for sample $x = 0.1$. Although the temperature range is very limited, we are able to fit the

inverse magnetization using the Curie–Weiss law, given by $\chi = C/(T - \theta)$, where C is the Curie constant and θ is the paramagnetic Curie temperature. The magnetization follows a Curie–Weiss law with a positive Curie temperature of 186, 182 and 170 K for samples $x = 0.05$, 0.1 and 0.15, respectively. The positive values of Curie temperature indicate the ferromagnetic interactions. For sample $x = 0.2$, a very confined range of fit due to experimental limitations makes it difficult to extract a precise value of C. The deduced Curie constant gives the value of the paramagnetic moment (P_{eff}). Theoretically, assuming that Mn^{3+} and Mn^{4+} are in a 1:1 ratio the P_{eff} is given as $P_{\text{eff}} = \sqrt{0.5 P_{\text{eff}}^2(\text{Mn}^{3+}) + 0.5 P_{\text{eff}}^2(\text{Mn}^{4+})}$, where P_{eff} for Mn^{3+} ($S = 2$) and for Mn^{4+} ($S = 3/2$) is 4.90 μ_B and 3.87 μ_B, respectively. This gives $P_{\text{eff}}^{\text{cal}} = 4.42$ μ_B, which is close to the experimentally determined value of 4.4 μ_B and 4.5 μ_B for samples $x = 0.10$ and 0.15, respectively.

The temperature dependence of resistivity for the La$_{0.5}$Ca$_{0.4}$Ba$_{0.1}$MnO$_3$ ($x = 0.1$) sample is displayed in figure 2(e) in the temperature range of 50–315 K. The data shown were collected during heating. No hysteresis behaviour between heating and cooling cycles is observed, suggesting that the transition from and to a charge ordered state is second order [44]. For samples $0.05 \leqslant x \leqslant 0.15$, the resistivity displays an insulating behaviour as the temperature is lowered and shows a steep rise at the charge ordering transition temperature. The charge ordering temperature T_{CO} was obtained from the minima of d(ln R)/dT versus temperature plots. The charge ordering temperature for all the samples in the composition range $0.05 \leqslant x \leqslant 0.15$ do not exhibit appreciable change and is $\sim$160 K. For the sample with $x = 0.2$, the charge ordering state is fully suppressed and

the sample exhibits a metal to insulator transition at $T_{MI} \sim$ 150 K, as shown in figure 3(e). It is observed that there is a difference between T_C and T_{MI} for the $x = 0.2$ sample, $\Delta T = T_C - T_{MI} = 30$ K. The observed difference may be attributed to the presence of isolated ferromagnetic clusters in the antiferromagnetic regime. As the temperature is reduced below T_C ferromagnetic clusters grow in size and develop a percolative path for conduction and therefore T_{MI} and T_C do not coincide. However, the other plausible explanation given in the literature is that the magnetic configuration on the grain surface is more chaotic than that in the core and thus the antiferromagnetic insulating regions appear near the grain boundaries. Such regions do not modify the magnetic transition temperature governed by the ferromagnetism of the grain core but can make the electrical transition shift to a lower temperature [45]. Figure 4(e) display the $\rho(T)$ for sample $x = 0.5$. At $x = 0.5$ the sample exhibits metallic behaviour below 280 K.

We attempt to describe the conduction mechanism in these compounds by fitting the $\rho(T)$ data to various models observed in charge ordered systems [46, 47]. For samples $0.05 \leqslant x \leqslant 0.15$, a change of slope is observed at $T_{CO} \sim 160$ K in $\rho(T)$ plots. Therefore, we have analysed the $\rho(T)$ behaviour by dividing it into two different regimes, namely (i) $T > 160$ K and (ii) $T < 160$ K. The first regime ($T > 160$ K) is the insulating region above T_{CO} where small polaron hopping is effective and the second regime ($T < 160$ K) is the charge ordered phase where a parallel combination of variable range hopping and small polaron hopping models is found to be valid.

When the particle–lattice interaction is strong enough, delocalized electrons or holes can be trapped in the potential well created by the displacement of an ion from its equilibrium position. The quasi-particles formed by the carriers and the lattice distortions are called polarons. When the carrier is localized within one unit cell then it is a small polaron. According to Emin and Holstein, resistivity in the small polaron regime is given as [48]

$$\rho_1 = CT \exp(W_A/k_B T) \quad (1)$$

where C is the resistivity coefficient $C = \frac{2}{3}\frac{k_B}{ne^2 a^2 \nu_{ph}}$, k_B is Boltzmann's constant, e is electronic charge, n is number density of charge carriers, a (≈ 3.9 Å) is the site-to-site hopping distance between two nearest-neighbouring Mn sites and ν_{ph} ($\approx 1.663 \times 10^{13}$ Hz) is the longitudinal optical phonon frequency associated with the principal mode of vibration of Mn–O bonds. The factor 2/3 takes into account the three-dimensional movement of polarons and W_A is the activation energy [49, 50]. The activation energy is given as $W_A = W_H + \frac{W_d}{2}$ for $T > \theta_D/2$, where W_H is the polaron hopping energy. W_d is the disorder energy arising due to the energy difference of neighbouring sites. W_d is significant at very low temperatures (at $T < \theta_D/4$) and is therefore neglected in the present analysis. We find $\rho(T)$ is well described by equation (1) in the region above T_{CO}. The fit is shown in inset (i) of figure 2(e) and in figure 3(e) for samples $x = 0.1$ and 0.2, respectively. From the fitted parameter we evaluate the number density of charge carriers or polaron density (n). This density of charge carriers (n) ranges from 2.1×10^{21} to

1.5×10^{21} cm^{-3}. It shows a minimum at $x = 0.1$. Also calculated is the activation energy, which has a maximum at $x = 0.1$. The value of n is in agreement with the reported study on manganites, where the order of magnitude varies between 10^{18} and 10^{23} cm^{-3}. Also, the activation energy ranges from 0.08 to 0.185 eV, and is comparable with the reported study on manganites [49, 51–55]. The activation energy W_A decreases continuously for compounds having $x > 0.1$, implying that the energy barriers to the polaron's motion are reduced as Ba concentration increases. In the adiabatic small polaron hopping the carriers adjusting rapidly to the motion of the lattice, on coincidence between energies of neighbouring sites, are likely to hop to the neighbouring sites [48, 49]. Therefore, this mechanism is expected to be prevalent at higher temperatures. Holstein's adiabatic model is based on the assumption that the polaron bandwidth J should satisfy the following condition [56]:

$$J > H \qquad \text{for adiabatic hopping and}$$

$$J < H \qquad \text{for non-adiabatic hopping conduction}$$

where $J \approx 0.67 h \nu_{ph} (\frac{T}{\theta_D})^{\frac{1}{4}}$ and $H \approx (\frac{2 k_B T W_H}{\pi})^{\frac{1}{4}}(\frac{h\nu_{ph}}{\pi})^{\frac{1}{2}}$.

The condition for small polaron formation is $J < W_H/3$, else there will be large polarons.

We calculate H and J at 300 K, for samples with $x \leqslant 0.15$. In all the calculations the Debye temperature θ_D is taken to be 516 K (determined for the $x = 0.5$ sample), assuming that it is not affected by Ba doping. For samples $x = 0.05$, 0.10 and 0.15 the values of H are 32.1, 32.2 and 31.5 meV, respectively. It is observed that $J(\approx 41 \text{ meV}) > H$ for samples $x \leqslant 0.15$, indicating an adiabatic hopping conduction mechanism occurring in these compounds. We also observe that $J < W_H/3$, implying that the conduction in samples with $x \leqslant 0.15$ is through small polaron hopping, in the adiabatic regime. The small polaron hopping conduction coupling constant is defined as $\gamma_p = 2W_H/h\nu_{ph}$. It is a measure of electron–phonon interactions in these manganites. According to Austin and Mott, if $\gamma_p > 4$, the electron–phonon interaction is strong [57–59]. However, in our case the coupling constant ranges from $\gamma_p \approx 4$–3.7, indicating intermediate electron–phonon interactions.

At low temperature, where the thermal energy is not great enough to allow electrons to hop to their nearest neighbours the conduction mechanism is mostly of variable range hopping type. In that case it is more favourable for the electrons to hop further to a site with lower energy difference. In the variable range hopping model, the temperature dependence of resistivity is described as [59]

$$\rho_2 = \rho_0 \exp(T_0/T)^{1/4} \quad (2)$$

where $T_0 = \frac{16}{k_B N(E_F)a^3}$ and $N(E_F)$ is the density of states at the Fermi level and a is the localization length reflecting the degree of localization of carriers. At low temperature ($T < 160$ K), however, the resistivity data when fitted to the variable range hopping model does not fit well in the whole temperature range below T_{CO}, indicating that there are other competing interactions at low temperatures. Since

Table 3. The parameters determined from fitting the resistivity data on both above and below T_{CO} and also in the metallic regime for samples La$_{0.5}$Ca$_{0.5-x}$Ba$_x$MnO$_3$.

x	$T < T_{CO}$		$T > T_{CO}$		Debye temperature θ_D (K)	Einstein temperature θ_E (K)
	T_O (K) $\times 10^8$	Activation energy (eV)	Polaron density n (cm^{-3}) $\times 10^{21}$	Activation energy (eV)		
0.05	9.23(8)	0.080(2)	2.1(2)	0.135(2)	—	—
0.10	8.83(10)	0.065(4)	1.50(1)	0.137(4)	—	—
0.15	2.4(3)	0.050(9)	1.80(9)	0.125(6)	—	—
0.20[a]	—	—	0.85(4)	0.108(9)	—	—
0.5	—	—	—	—	516(30)	642(15)

[a] Sample $x = 0.2$ is not a charge ordered system: however, in the insulating regime it fits to the adiabatic small polaron hopping model [72]. For $x = 0.5$ sample, $\rho_0 = 0.0226(1)$ (Ω cm), $\rho_1 = 17.3(5)$ (Ω cm K^{-1}), $\rho_2 = 0.0178(2)$ (Ω cm) and $\rho_3 = 0.41(2) \times 10^{-5}$ (Ω cm K$^{-3/2}$).

there exists a possibility of coexistence of ferromagnetic and antiferromagnetic clusters as observed for the parent compound [35], the resistivity below T_{CO} can be considered as a parallel combination of variable range hopping and small polaron hopping models [60, 61]. Therefore the resistivity can be described by the following formula:

$$\frac{1}{\rho} = \frac{1}{\rho_1} + \frac{1}{\rho_2} \qquad (3)$$

where ρ_1 is the resistivity from the small polaron hopping model and ρ_2 is the corresponding resistivity of the variable range hopping model. The fit described by equation (3) is shown in inset (ii) of figure 2(e). In the charge ordered region, the resistivity is described by a parallel combination of two different hopping mechanisms; it is observed that the activation energies as well as the values of T_0 decrease continuously. According to the equation defining T_0 given in the text above, as T_0 decreases for a constant value of a, the density of states $N(E_F)$ at the Fermi level increases. The values of T_0 observed by us are in agreement with previous reports [61].

Figure 4(e) displays $\rho(T)$ for the sample $x = 0.5$ and the continuous line is fitted to the data. For this sample, we fitted the resistivity data in the metallic regime using the equation shown below [62]:

$$\rho(T) = \rho_0 + \frac{\rho_1}{\theta_D} \left(\frac{T}{\theta_D}\right)^5 \int_0^{\frac{\theta_D}{T}} \frac{z^5 \, dz}{(e^z - 1)(1 - e^{-z})}$$
$$+ \rho_2 \left[\frac{T}{\theta_E} \sinh^2\left(\frac{\theta_E}{2T}\right)^{-1}\right] + \rho_3 T^{3/2}. \qquad (4)$$

Here the first temperature-independent term is residual resistivity due to the defect scattering, the second term is the contribution from the interaction of electrons with the acoustic phonons, the third term is associated with the interaction of electrons with the optical phonons and the fourth term is associated with electron–magnon scattering [62–64]. An acoustic Debye branch is characterized by the Debye temperature θ_D and an optical peak is defined by the Einstein temperature θ_E [65]. In a simple metal, lattice vibrations are described by the acoustic modes as usually only one atom exists in the primitive cell. The second term in equation (4) describes lattice vibration due to acoustic modes. However, in oxides there are at least two atoms in the unit

cell and optical modes are also active. When the scattering occurs independently, then according to Matthiessen's rule the resistivity is the sum of all the independent terms as described in equation (4). The coefficients ρ_1, ρ_2, ρ_3, residual resistivity ρ_0, θ_D and θ_E are the fitting parameters for the $x = 0.5$ sample. The electron–magnon scattering term is found to be proportional to T^2 and $T^{3/2}$ for single-particle excitation and collective-particle excitation, respectively [63, 64]. Our data gives a better fit for the $T^{3/2}$ term as compared to the T^2 term. The values of θ_D and θ_E are found to be in agreement with those reported in the literature [66–68]. The parameters obtained from the fitted models described above are summarized in table 3.

The inset of figure 3(e) shows the minimum in resistivity for sample $x = 0.2$. Similar behaviour at low temperature is observed for all samples having $x \geqslant 0.2$, with $T_{MIN} \sim 25$ K. The resistivity minimum could be magnetic in origin (Kondo effect) or due to disorder (electron–electron scattering). The strong magnetic nature of the samples rules out the Kondo effect. This is also evident from the invariance of T_{MIN} with x, although T_C increases.

Our transport studies have shown a transition from insulating to metallic state for samples $x \geqslant 0.2$. A recent study by Sen *et al* have investigated the insulator to metal transition phenomena in manganites by Monte Carlo simulation techniques [69]. Disorder is modelled as a form of random local energy. It was found that, while the ferromagnetic metallic state was not affected by disorder, the charge ordered insulating state was significantly affected by it. In the clean limit, i.e. in the absence of disorder, the density of states (DOS) showed a gap at the chemical potential, which closed with an increase in disorder. We observe a similar behaviour for DOS obtained experimentally by fitting the resistivity data described above.

3.3. Magnetic structure

The neutron diffraction pattern for samples $x = 0.1$ and 0.15 at 22 K is shown in figure 6. The neutron diffraction pattern for sample $x = 0.1$ is representative of all the samples with $x \leqslant 0.1$. At 22 K, superlattice reflections for samples $x = 0.1$ and 0.15 are observed and are marked with asterisks (∗) and plus (+) symbols in figure 6. For the $x = 0.1$ sample, superlattice reflections are indexed on a $2a \times b \times 2c$ cell with

the space group $P2_1/m$. In particular, reflections $(0, 1, \frac{1}{2})$ and $(\frac{1}{2}, 1, \frac{1}{2})$ are shown with asterisks in figure 6, characteristic of a CE-type antiferromagnetic spin structure and are evident below $\sim$100 K for samples with $x \leqslant 0.1$. In this structure, Mn occupies two distinct sites for Mn^{3+} and Mn^{4+}. The Mn^{3+} and Mn^{4+} sublattice is associated with a propagation vector $(0, 0, \frac{1}{2})$ and $(\frac{1}{2}, 0, \frac{1}{2})$, respectively [3]. On refinement of the diffraction pattern for sample $x = 0.1$ at 22 K, the magnetic moments obtained on Mn^{3+} and Mn^{4+} sites are 1.8(1) and 2.1(1) μ_B/Mn, respectively. Additionally, no enhancement of intensity in low-angle fundamental Bragg reflections was visible, indicating the absence of ferromagnetic ordering observable from a neutron diffraction experiment. However, $M(H)$ curves shown in figure 5 do show a signature of ferromagnetism at these temperatures. However, the moment values are too small to influence the diffraction pattern. This observation in conjunction with $M(H)$ behaviour indicates the coexistence of ferromagnetic and antiferromagnetic phases. For the sample $x = 0.15$, superlattice reflections, in addition to the reflections corresponding to CE-type AFM spin structure, are observed. These reflections could be indexed in an $a \times 2b \times c$ cell in the $P\bar{1}$ space group and were identified with A-type AFM spin structure. Thus, in the $x = 0.15$ compound the low temperature antiferromagnetic state is a mixture CE-type and A-type spin structure, as shown in figure 6. Some of the strong superlattice reflections corresponding to these respective structures are highlighted in figure 6. The CE-type antiferromagnetic structure is the same as described above for sample $x = 0.1$. The refined antiferromagnetic moment for the $x = 0.15$ sample of the A-type antiferromagnetic phase at 22 K is 1.53(5) μ_B/Mn and is oriented ferromagnetically in the ac plane and antiferromagnetically coupled along the b axis. The A-type structure observed in this sample is similar to that reported previously for Sr-doped compounds, albeit the A-type structure for Sr-doped compounds is observed at higher concentrations of Sr [14]. The inset in figure 6 displays the temperature dependence of moment for Mn^{3+} and Mn^{4+} ions for sample $x = 0.1$. Both the Mn site moments have identical transition temperatures ($\sim$100 K). From the temperature dependence of the refined Mn site magnetic moment we obtain the value of T_N. Within $\pm$12 K, the T_N is invariant with x. Figure 7 displays the neutron diffraction pattern for sample $x = 0.2$ obtained at 22 and 300 K. This figure is representative for all samples in the range $x \geqslant 0.2$. For samples $x \geqslant 0.2$, significant enhancement in intensity of low-angle nuclear reflection (0 2 0) and (1 0 1) is observed. This is a clear indication of ferromagnetic ordering in these samples. This ferromagnetic phase is fitted in orthorhombic structure in the $Pnma$ space group. The ferromagnetic transition temperature for $x = 0.2$ is $\sim$180 K. The inset in figure 7 shows the temperature dependence of ferromagnetic moment for sample $x = 0.2$ and the continuous line is a Brillouin function fit with $T_C \approx 180$ K, $S = 1.75$. The sample $x = 0.5$, exhibits the signature of ferromagnetism at all temperature up to 325 K. Mallik *et al* have reported its $T_C \approx 340$ K [25]. Our results are in contradiction with the reported T_C of $\sim$237 K in the A-site disordered $La_{0.5}Ba_{0.5}MnO_3$ compound [20]. Figure 4(d) shows the temperature dependence for magnetic moments obtained
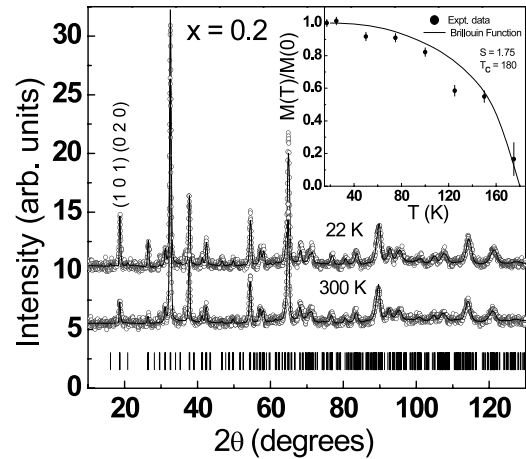

Figure 7. Neutron diffraction pattern for $La_{0.5}Ca_{0.3}Ba_{0.2}MnO_3$ ($x = 0.2$) at 22 and 300 K. Continuous lines are the fitted lines to the chemical and magnetic structure discussed in the text. The tick marks show the position of the Bragg reflections in $Pnma$ space group. The inset shows the variation of ferromagnetic moment with temperature. The continuous line is a fit to the Brillouin function.

from refinement of the neutron diffraction pattern at various temperatures. The continuous line is a fit to the Brillouin function with $T_C \approx 340$ K, $S = 3/2$. The ferromagnetic moment at 22 K for the $x = 0.5$ sample is 3.59(7) μ_B/Mn and compares well with the expected value of 3.5 μ_B/Mn. The fitting parameters at 22 K for all the samples are summarized in table 2.

The CE-type model used for refinement describes the low temperature phase as a one-dimensional zigzag chain of ferromagnetically coupled Mn spins in the ac plane and the chains in turn are coupled antiferromagnetically to each other. This is the checkerboard pattern, showing two nonequivalent crystallographic sites present in the low temperature phase of $La_{0.5}Ca_{0.5}MnO_3$ for the Mn atom as supported by Radaelli *et al* [10]. Recent experimental and theoretical studies reveal that the ionic picture of Mn^{3+} and Mn^{4+} atoms may not be correct. Herrero-Martín *et al* have probed the local structure around the Mn ion using resonant scattering of a synchrotron x-ray beam. Two different Mn sites are found. However, the charge difference between the two configurations is found to be only 0.16 electrons [70]. From the refinement of our data we are not able to ascribe two different sites for Mn ions below the T_{CO}. However, the near identical values of moment on Mn^{3+} and Mn^{4+} suggest that the charge difference may not be 1 as suggested by Herrero-Martín *et al* [70].

We summarize all the experimental results discussed above in the form of a phase diagram shown in figure 8. The phase diagram is constructed as a function of $\langle r_A \rangle$. At low temperature, charge ordered CE-type antiferromagnetic phase is evident. Beyond $\langle r_A \rangle = 1.227$ Å, in addition to the charge ordered CE-type antiferromagnetic phase, an A-type antiferromagnetic phase also emerges. Finally, above $\langle r_A \rangle = 1.241$ Å, the charge ordered state is destroyed and a ferromagnetic phase emerges. The evolution of phases as a function of temperature can be discussed over two distinct regimes, namely $\langle r_A \rangle \leqslant 1.241$ Å and $\langle r_A \rangle \geqslant 1.241$ Å. In
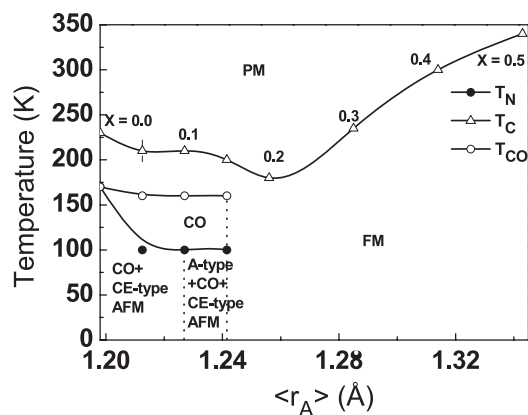
Figure 8. Magnetic phase diagram of the $La_{0.5}Ca_{0.5-x}Ba_xMnO_3$ system as a function of temperature and average A-site ionic radii $\langle r_A \rangle$. The abbreviations in the figure imply FM: ferromagnetic, PM: paramagnetic, CO: charge ordering, OO: orbital ordering, AFM: antiferromagnetic phases.

the first regime, the antiferromagnetism of CE-type, A-type or both phases coexist below T_N. In the temperature region below 160 K, a charge ordered phase exists. In the second regime ($\langle r_A \rangle \geqslant 1.241$ Å), ferromagnetic ordering exists for all temperatures below T_C. We find that, with increasing $\langle r_A \rangle$, T_N shows a reduction from 170 to 100 K and thereafter remains constant. The ferromagnetic transition temperature reduces slightly, reaching a minimum at 180 K for $\langle r_A \rangle = 1.256$ Å ($x = 0.2$). Thereafter, T_C increases again to 340 K at $x = 0.5$. This may be compared with the effect of disorder in CMR materials. In these, an increase in disorder leads to a rapid reduction in T_C. This phase diagram may be compared with that obtained from computational studies by Pradhan *et al* [30]. The effect of varying Ca/Ba ratio and its influence on the magnetic phase diagram is observed to be similar to that of varying the exchange J_{AF} between t_{2g} spins for intermediate values of λ. From resistivity studies we infer that electron–phonon coupling is in the intermediate regime. In this range of λ the phase diagram exhibits a transition from CE–OO–CO antiferromagnetic to FM–OD–CD as a function of increasing J_{AF}. Experimentally we observe similar behaviour for Ba-doped samples reported here and as well as for Sr-doped samples previously reported [14]. In comparison to Sr-doped samples, increase in ionic radii in the present case leads to large shrinkage in the antiferromagnetic phase. The ferromagnetic phase sets in for much lower values of x. We associate this nature of the phase diagram with increased disorder σ^2 in this system. However, as compared to ordered structure as reported in $LaBaMn_2O_6$ [71] where disordering a CO–OO–CE-type antiferromagnetic phase leads to a transition to a spin glass phase, we always find that melting of the CE-type antiferromagnetic structure proceeds through numbers of long range ordered structures.

4. Conclusion

All the samples studied in the series $La_{0.5}Ca_{0.5-x}Ba_xMnO_3$ ($0 < x \leqslant 0.5$) crystallize in orthorhombic structure (*Pnma*

space group) and do not exhibit any structural transition on lowering of temperature. Increasing x leads to an increase in $\langle r_A \rangle$ and cation size disorder (σ^2). These are found to strongly influence the transport and magnetic properties across the series of samples. The CE type of magnetic structure is found to be unstable and exists only for low doping of x ($\leqslant 0.10$). With increase in $\langle r_A \rangle$ and σ^2, at $x = 0.15$ the magnetic structure is a mixture of CE type and A type. Orbital ordering in addition to spin and charge ordering is observed in all samples with $x \leqslant 0.15$. At $x \geqslant 0.2$, a ferromagnetic metallic state is observed. The ferromagnetic transition temperature increases with increase in x. The antiferromagnetic phase is confined to much lower doping of Ba as compared to Sr-doped compounds reported earlier [14] and is attributed to a large increase in disorder, σ^2.

The temperature dependence of resistivity shows that the low temperature charge ordered insulating state is destroyed as Ba concentration is increased and the system becomes metallic. For samples $x \leqslant 0.15$, below T_{CO} (~ 160 K), the temperature dependence of resistivity is described by a parallel combination of adiabatic small polaron hopping and variable range hopping mechanisms. Above T_{CO} conduction is through adiabatic hopping of small polarons. In the metallic region resistivity data follows the Bloch–Grüneisen model together with contributions from high frequency optical phonons and magnetic scattering.

References

[1] Rao C N R and Raveau B 1998 *Colossal Magnetoresistance, Charge Ordering, and Related Properties of Manganese Oxides* (Singapore: World Scientific)
[2] Pissas M and Kallias G 2003 *Phys. Rev.* B **68** 134414
[3] Radaelli P G, Cox D E, Marezio M and Cheong S-W 1997 *Phys. Rev.* B **55** 3015
[4] Rodriguez-Martinez L M and Attfield J P 1998 *Phys. Rev.* B **58** 2426
[5] Dagotto E, Hotta T and Moreo A 2001 *Phys. Rep.* **344** 1
[6] Hwang H Y, Cheong S W, Radaelli P G, Marezio M and Batlogg B 1995 *Phys. Rev. Lett.* **75** 914
[7] Rodriguez-Martinez L M, Ehrenberg H and Attfield J P 2000 *Solid State Sci.* **2** 11
[8] Zhou J P, McDevitt J T, Zhou J S, Yin H Q, Goodenough J B, Gim Y and Jia Q X 1999 *Appl. Phys. Lett.* **75** 1146
[9] Raveau B, Maignan A and Caignaert V 1995 *J. Solid State Chem.* **117** 224
[10] Radaelli P G, Marezio M, Hwang H Y and Cheong S W 1996 *J. Solid State Chem.* **122** 444
[11] Mahesh R, Mahendiran R, Raychaudhuri A K and Rao C N R 1995 *J. Solid State Chem.* **120** 204
[12] Rodriguez-Martinez L M and Attfield J P 1996 *Phys. Rev.* B **54** R15622
[13] Shannon R D 1967 *Acta Crystallogr.* A **32** 751
[14] Dhiman I, Das A, Mishra P K and Panicker L 2008 *Phys. Rev.* B **77** 094440
[15] Autret C, Martin C, Hervieu M, Maignan A, Raveau B, André G, Bourée F and Jirak Z 2004 *J. Magn. Magn. Mater.* **270** 194
[16] Autret-Lambert C, Gervais M, Gervais F, Simon P and Raimboux N 2005 *Solid State Sci.* **7** 1035
[17] Damay F, Martin C, Maignan A and Raveau B 1997 *J. Appl. Phys.* **82** 6181
[18] Autret C, Martin C, Hervieu M, Maignan A, Raveau B, André G, Bourée F and Jirak Z 2003 *Chem. Mater.* **15** 1886

[19] Vanitha P V and Rao C N R 2001 *J. Phys.: Condens. Matter* **13** 11707

[20] Chmaissem O, Dabrowski B, Kolesnik S, Mais J, Suescun L and Jorgensen J D 2006 *Phys. Rev.* B **74** 144415

[21] Moritomo Y, Kuwahara H, Tomioka Y and Tokura Y 1997 *Phys. Rev.* B **55** 7549

[22] Zhu D, Cao P, Liu W, Ma X, Maignan A and Raveau B 2007 *Mater. Lett.* **61** 217

[23] Smolyaninova V N, Lofland S E, Hill C, Budhani R C, Gonen Z S, Eichhorn B W and Green R L 2002 *J. Magn. Magn. Mater.* **248** 348

[24] Yuan S L, Tu F, Yang Y P, Zeng X Y, Zhang G Q, Peng G, Liu J, Jiang Y, Li Z Y, Xiong C S, Xiong W H and Tang C Q 2001 *Phys. Status Solidi* a **185** 391

[25] Mallik R, Reddy E S, Paulose P L, Majumdar S and Sampathkumaran E V 1999 *J. Phys.: Condens. Matter* **11** 4179

[26] Moreo A, Yunoki S and Dagotto E 1999 *Science* **283** 2034

[27] van den Brink J, Khaliullin G and Khomskii D 1999 *Phys. Rev. Lett.* **83** 5118

[28] Brey L 2005 *Phys. Rev.* B **71** 174426

[29] Moreo A, Mayr M, Feiguin A, Yunoki S and Dagotto E 2000 *Phys. Rev. Lett.* **84** 5568

[30] Pradhan K, Mukherjee A and Majumdar P 2007 *Phys. Rev. Lett.* **99** 147206

[31] Rodriguez-Carvajal J 1992 *Physica* B **192** 55

[32] Jirak Z, Krupicka S, Simsa Z, Dlouha M and Vratislav S 1985 *J. Magn. Magn. Mater.* **53** 153

[33] Arulraj A, Dinnebier R E, Carlson S, Hanfland M and Smaalen S v 2007 *Prog. Solid State Chem.* **35** 367

[34] Glazer A M 1972 *Acta Crystallogr.* B **28** 3384

[35] Radaelli P G, Cox D E, Marezio M, Cheong S-W, Schiffer P E and Ramirez A P 1995 *Phys. Rev. Lett.* **75** 4488

[36] Kennedy B J, Howard C J and Chakoumakos B C 1999 *J. Phys.: Condens. Matter* **11** 1479

[37] Goodenough J B and Longo J M 1970 *Landolt–Bornstein Tabellen, New Series* vol III/4a (Berlin: Springer)

[38] Maris G, Volotchaev V and Palstra T M 2004 *New J. Phys.* **6** 153

[39] Medarde M, Mesot J, Lacorre P, Rosenkranz S, Fischer P and Gobrecht K 1995 *Phys. Rev.* B **52** 9248

[40] Arulraj A, Santhosh P N, Gopalan R S, Guha A, Raychaudhuri A K, Kumar N and Rao C N R 1998 *J. Phys.: Condens. Matter* **10** 8497

[41] Goodenough J B 1955 *Phys. Rev.* **100** 564

[42] Das A, Babu P D, Chatterjee S and Nigam A K 2004 *Phys. Rev.* B **70** 224404

[43] Loudon J C, Mathur N D and Midgley P A 2002 *Nature* **420** 19

[44] Schiffer P, Ramirez A P, Bao W and Cheong S W 1995 *Phys. Rev. Lett.* **75** 3336

[45] Huang Y H, Yan C H, Wang Z M, Liao C S and Xu G X 2001 *Solid State Commun.* **118** 541

[46] Mott N F 1990 *Metal–Insulator Transitions* (London: Taylor and Francis)

[47] Sarathy K V, Parashar S, Raju A R and Rao C N R 2002 *Solid State Sci.* **4** 353

[48] Emin D and Holstein T 1960 *Ann. Phys.* **53** 439

[49] Quenneville E, Meunier M, Yelon A and Morin F 2001 *J. Appl. Phys.* **90** 1891

[50] Machida A, Moritomo Y and Nakamura A 1998 *Phys. Rev.* B **58** R4281

[51] Liu X, Zhu H and Zhang Y 2001 *Phys. Rev.* B **65** 024412

[52] Nair S and Banerjee A 2006 *J. Phys.: Condens. Matter* **16** 8335

[53] Philip J and Kutty T R N 1999 *J. Phys.: Condens. Matter* **11** 8537

[54] Worledge D C, Snyder G J, Beasley M R, Geballe T H, Hiskes R and DiCarolis S 1996 *J. Appl. Phys.* **80** 5158

[55] Sun Y, Xu X, Zheng L and Zhang Y 1999 *Phys. Rev.* B **60** 12317

[56] Holstein T 1959 *Ann. Phys.* **8** 343

[57] Austin I G and Mott N F 1969 *Adv. Phys.* **18** 41

[58] Mott N F 1968 *J. Non-Cryst. Solids* **1** 1

[59] Mott N F and Davis E A 1979 *Electronic Processes in Non Crystalline Materials* 2nd edn (Oxford: Clarendon)

[60] Sun Y, Xu X and Zhang Y 2000 *J. Phys.: Condens. Matter* **12** 10475

[61] Zhou H D, Zheng R K, Li G, Feng S J, Liu F, Fan X J and Li X G 2002 *Eur. Phys. J.* B **26** 467

[62] Rosenberg H M 1965 *Low Temperature Solid State Physics* (Oxford: Oxford University Press)

[63] Bergmann G and Marquardt P 1978 *Phys. Rev.* B **17** 1355

[64] Kaul S N, Kettler W and Rosenberg M 1986 *Phys. Rev.* B **33** 4987

[65] Varshney D and Kaurav N 2004 *Eur. Phys. J.* B **40** 129

[66] Mollah S, Huang H L, Yang H D, Pal S, Taran S and Chaudhuri B K 2004 *J. Magn. Magn. Mater.* **284** 383

[67] Ibarra M R, Algarabe P A, Marquina C, Blasco J and Garcia J 1995 *Phys. Rev. Lett.* **75** 3541

[68] Salamon M and Jaime M 2001 *Rev. Mod. Phys.* **73** 583

[69] Şen C, Alvarez G and Dagotto E 2004 *Phys. Rev.* B **70** 064428

[70] Herrero-Martín J, García J, Subías G, Blasco J and Sánchez M C 2004 *Phys. Rev.* B **70** 024408

[71] Chmaissem O, Dabrowski B, Kolesnik S, Mais J, Jorgensen J D, Short S, Botez C E and Stephens P W 2005 *Phys. Rev.* B **72** 104426

[72] Amelitchev V A, Guttler B, Gorbenko O Y, Kaul A R, Bosak A A and Ganin A Y 2001 *Phys. Rev.* B **63** 104430